Science Advances
AAAS

advances.sciencemag.org/cgi/content/full/7/1/eabb3594/DC1

Supplementary Materials for

Multidimensional coherent spectroscopy reveals triplet state coherences in cesium lead-halide perovskite nanocrystals

Albert Liu, Diogo B. Almeida, Luiz G. Bonato, Gabriel Nagamine, Luiz F. Zagonel, Ana F. Nogueira, Lazaro A. Padilha*, S. T. Cundiff*

*Corresponding author. Email: padilha@ifi.unicamp.br (L.A.P.); cundiff@umich.edu (S.T.C.)

Published 1 January 2021, *Sci. Adv.* **7**, eabb3594 (2021)
DOI: 10.1126/sciadv.abb3594

This PDF file includes:

Sample Synthesis

Synthesis of the nanocrystals used in this study follows the procedure detailed in (1).

Preparation of Cs-Oleate Stock Solution

80 mg of Cs_2CO_3 (0.5 mM Cs^+) was added to a 50 mL 2-neck round-flask, followed by addition of 1 mL of oleic acid and 7 mL of 1-octadecene. The flask was connected to a Schlenk line and vigorously stirred under vacuum at 100°C for 1 hour. After obtaining a transparent solution ($[Cs^+]$ = 0.06 mol/L), the system was maintained at 80°C under nitrogen flow to avoid the formation of a white precipitate.

Synthesis of $CsPbI_3$ Perovskite Nanocrystals with Cs:Pb:I = 1:4.34:8.68 Molar Ratio

100 mg of PbI_2 (~ 0.217 mM) was added to a 50 mL 3-neck round-flask, followed by the addition of 4.5 mL of 1-octadecene. The flask was connected to a Schlenk line and vigorously stirred under vacuum at 100°C for 30 minutes. Afterwards 1 mL of oleic acid and 0.l5 mL of oleylamine was added, while keeping the reaction flask under vigorous stirring in vacuum at 100°C until complete solubilization of the PbI_2, upon obtaining a transparent yellow solution. Prior to injection of the Cs^+ precursor, the temperatures of the Pb^{2+} and I^- precursor solutions were raised to 140°C under vigorous stirring and nitrogen flow, followed by swift injection of 0.8 mL of Cs-oleate stock solution. Formation of an intense red colloidal suspension of $CsPbI_3$ nanocrystals was then observed. The suspension was immediately submerged in a cold-water bath to cool down to room temperature for quenching nanocrystal growth.

The nanocrystals were cleaned by adding 15 mL of anhydrous methylacetate and centrifuged at 12000 rpm for 5 minutes. The supernatant was discarded and the precipitated nanocrystals were redispersed in anhydrous hexane.

Triplet State Quantum Pathways and Feynman Diagrams

Peak structures in multi-dimensional spectra of a material are interpreted in terms of the accessible quantum pathways of its third-order optical response. These quantum pathways are readily enumerated by use of double-sided Feynman diagrams, which also provide a straightforward method to predict their associated peak position in a multi-dimensional spectrum. The rules for constructing and interpreting double-sided Feynman diagrams are discussed in detail elsewhere (16, 22) so we present only a brief summary here.

All possible double-sided Feynman diagrams for the triplet-state manifold considered here are shown in Fig. S1. These diagrams consist of vertically-arranged sequences of density matrix elements, beginning with an initial ground state population $|g\rangle\langle g|$ as time advances upwards, with changes in the density matrix Bra/Ket induced by interactions with each excitation pulse (represented by arrows). For the signal wavevector $\mathbf{k}_{sig} = -\mathbf{k}_A + \mathbf{k}_B + \mathbf{k}_C$ measured here, there are four arrows in total consisting of initial and final leftward pointing arrows and two intermediate rightward pointing arrows. An arrow pointing (out-)inward corresponds to (de-)excitation of the corresponding Bra/Ket, resulting in three types of quantum pathways termed excited-state emission (ESE), ground-state bleach (GSB), and excited-state absorption (ESA). Here we consider only ESE and GSB pathways, since ESA pathways involve emission from biexciton states that manifest as asymmetric sidebands located outside our region of interest at the biexciton binding energy.

Peak Strength Calculations in the Nanocrystal Reference Frame

To explain the observed peak structure, we theoretically calculate relative peak strengths in the nanocrystal reference frame as shown in Fig. S2.

To do so, we calculate the peak positions and strengths of all quantum pathways shown in Fig. S1. First, the absorption and emission energy peak coordinates are determined by the first and last coherences of each Feynman diagram and their oscillation frequencies. Second, the peak strengths are determined by the dipole matrix element $|\vec{d}_i| = d_i$ of each light-matter interaction and the relative spatial orientations of each transition dipole moment $\vec{d}_i$. We make one simplifying assumption, namely that each nanocrystal is orientated such that at least one of their triplet state dipole moments is oriented along the initial excitation pulse polarization. This assumption is justified in the last paragraph of this section.

Calculated peak strengths are shown in Figs. S2C and S2D for normalized dipole matrix elements $d_x = d_z = 1$ and varying d_y. The angle θ_{xy} between $\vec{d}_x$ and $\vec{d}_y$ is also varied between 0° and 45° as shown in Fig. S2B. As shown by the lowest peak strength plot, we achieve the best agreement with our experimental results by modeling a stronger dipole moment $d_y = 1.5$ and a finite angle $\theta_{xy} = 45°$.

We note that more rigorous modeling of the relative peak strengths would require calculating the rotationally-averaged optical response function in the laboratory reference frame. However, dipole selection rules have been shown to persist in a rotationally-averaged nanocrystal ensemble (35) and does not affect dephasing rates or inhomogeneous broadening of transitions. As an example, this can be intuitively understood by considering the strengths of peaks 1-3 for co-linear excitation and a nanocrystal orientation shown in Fig. S3A. As the nanocrystal rotates in the $\vec{d}_x$ - $\vec{d}_y$ plane (as θ_{NC} increases), the ratio between the central and sideband peak strengths decreases. Importantly however, the overall nonlinear signal also decreases which indicates that the nonlinear signal is predominantly generated by nanocrystals whose dipole moments are oriented along the excitation polarization. We thus expect the effects of rotational averaging to modify the peak strengths calculated here without affecting our main conclusions.

Resonance Lineshapes in One- and Zero-Quantum Spectra

We show straightforward extensions of the procedure outlined by Siemens et al. (27) to fit lineshapes of sidebands in one-quantum and zero-quantum spectra.

One-Quantum Lineshapes

We consider the case of a rephasing signal resulting from excitation and emission frequencies ω_1 and ω_2 respectively (ignoring dynamics during T), and assume perfectly correlated inhomogeneous broadening between the two transitions with dephasing rates γ_1 and γ_2:

$$s(t,\tau) = \Theta(t)\Theta(\tau)e^{-\gamma_1\tau}e^{-\gamma_2 t}\int e^{-i[(\omega_1+\Delta\omega)\tau-(\omega_2+\Delta\omega)t]}e^{-\frac{\Delta\omega^2}{2\sigma^2}}d\Delta\omega$$

$$= \Theta(t)\Theta(\tau)e^{-\gamma_1\tau}e^{-\gamma_2 t}e^{-i\omega_1\tau}e^{+i\omega_2 t}\,\mathcal{F}\left\{e^{-\frac{\Delta\omega^2}{2\sigma^2}}\right\}\Big|_{t-\tau}$$

$$\propto \Theta(t)\Theta(\tau)e^{-\gamma_1\tau}e^{-\gamma_2 t}e^{-i\omega_1\tau}e^{+i\omega_2 t}e^{-\frac{\sigma^2}{2}(t-\tau)^2}$$

Defining the new time variables:

$$t' = \frac{1}{2}(t+\tau) \qquad \tau' = \frac{1}{2}(t-\tau)$$

We recast the time-domain signal:

$$s(t',\tau') = \Theta(t'+\tau')\Theta(t'-\tau')e^{-\gamma_1(t'-\tau')}e^{-\gamma_2(t'+\tau')}e^{-i\omega_1(t'-\tau')}e^{+i\omega_2(t'+\tau')}e^{-2\sigma^2\tau'^2}$$

It is important to determine the specific axes that the new time variables result in after Fourier transform. Writing out the original transform:

$$f(t,\tau) = \iint e^{-i(\omega_t t+\omega_\tau\tau)}f(\omega_t,\omega_\tau)d\omega_\tau d\omega_t$$

In terms of the new time variables:

$$f(t',\tau') = \iint e^{-i[\omega_t(t'+\tau')+\omega_\tau(t'-\tau')]}f(\omega_t,\omega_\tau)d\omega_\tau d\omega_t$$

$$= \iint e^{-i[(\omega_t+\omega_\tau)t'+(\omega_t-\omega_\tau)\tau']}f(\omega_t,\omega_\tau)d\omega_\tau d\omega_t$$

We see that the natural conjugate variables for t' and τ' are:

$$\omega_{t'} = \omega_t + \omega_\tau \qquad \omega_{\tau'} = \omega_t - \omega_\tau$$

or equivalently:

$$\omega_t = \omega_{t'} + \omega_{\tau'} \qquad \omega_\tau = \omega_{t'} - \omega_{\tau'}$$

Note that in the rephasing pulse sequence, ω_τ is negative.

Using the Jacobian of our variable transformation:

$$J = \begin{vmatrix} d\omega_t/d\omega_{t'} & d\omega_t/d\omega_{\tau'} \\ d\omega_\tau/d\omega_{t'} & d\omega_\tau/d\omega_{\tau'} \end{vmatrix} = -1 - 1 = -2$$

We change the variables of integration:

$$f(t',\tau') = 2\iint e^{-i(\omega_{t'}t'+\omega_{\tau'}\tau')}f(\omega_{t'},\omega_{\tau'})d\omega_{\tau'}d\omega_{t'}$$

We now shift the signal to the origin in our t' and τ' coordinates via multiplication by $e^{+i\omega_1(t'-\tau')\tau'}e^{-i\omega_2(t'+\tau')}$:

$$s_{origin}(t',\tau') = \Theta(t'+\tau')\Theta(t'-\tau')e^{-\gamma_1(t'-\tau')}e^{-\gamma_2(t'+\tau')}e^{-2\sigma^2\tau'^2}$$

The projections along t' and τ' are then:

$$s_{proj,t'} = \int_{-\infty}^{\infty} s_{origin}(t',\tau')d\tau' = e^{-(\gamma_1+\gamma_2)t'\int_{-t'}^{t'} e^{(\gamma_1-\gamma_2)\tau'} e^{-2\sigma^2\tau'^2} d\tau'}$$

$$s_{proj,\tau'} = \int_{-\infty}^{\infty} s_{origin}(t',\tau')dt' = e^{(\gamma_1-\gamma_2)\tau' e^{-2\sigma^2\tau'^2}\int_{|\tau'|}^{\infty} e^{-(\gamma_1+\gamma_2)t'}} dt'$$

Where the Heaviside functions are accounted for by change of integration limits.

In the inhomogeneous limit ($\sigma \gg \gamma_1, \gamma_2$) the signal decays along τ' much faster than along t'. In the integral along τ' we can approximate the gaussian portion of the kernel as a delta function. In the integral along t', we can approximate the lower limit as 0. These two limits give:

$$s_{proj,t'} = e^{-(\gamma_1+\gamma_2)t'\int_{-t'}^{t'} e^{(\gamma_1-\gamma_2)\tau'}} \delta(\tau')d\tau' = e^{-(\gamma_1+\gamma_2)t'}\Theta(t')$$

$$s_{proj,\tau'} = e^{(\gamma_1-\gamma_2)\tau' e^{-2\sigma^2\tau'^2}\int_0^{\infty} e^{-(\gamma_1-\gamma_2)t'}} dt' = e^{(\gamma_1-\gamma_2)\tau' e^{-2\sigma^2\tau'^2}}$$

which then give the frequency domain lineshapes in the inhomogeneous limit:

$$S_{slice}(\omega_{t'}) \propto \frac{1}{(\gamma_1+\gamma_2)+i\omega_{t'}} \qquad (Cross-Diagonal)$$

$$S_{slice}(\omega_{\tau'}) \propto e^{-\frac{\omega_{\tau'}^2}{8\sigma^2}} \qquad (Diagonal)$$

where we've assumed $\gamma_1 - \gamma_2 \ll \sigma$.

<u>Zero-Quantum Lineshapes</u>

The lineshapes of a zero-quantum spectrum can be derived by the same method, with inclusion of an intermediate zero-quantum coherence with a dephasing rate of γ_T that is determined by the correlation between the two optical frequency energy gap fluctuations:

$$s(t,T,\tau) = \Theta(t)\Theta(T)\Theta(\tau)e^{-\gamma_1\tau}e^{-\gamma_2 t}e^{-\gamma_T T}\int e^{-i[(\omega_1+\Delta\omega)\tau-(\omega_2+\Delta\omega)t]}e^{i(\omega_2-\omega_1)T}e^{-\frac{\Delta\omega^2}{2\sigma^2}}d\Delta$$

$$= \Theta(t)\Theta(T)\Theta(\tau)e^{-\gamma_1\tau}e^{-\gamma_2 t}e^{-\gamma_T T}e^{+i(\omega_2-\omega_1)T}e^{-i\omega_1\tau}e^{+i\omega_2 t}\int e^{+i\Delta\omega(t-\tau)}e^{-\frac{\Delta\omega^2}{2\sigma^2}}d\Delta$$

$$= \Theta(t)\Theta(T)\Theta(\tau)e^{-\gamma_1\tau}e^{-\gamma_2 t}e^{-\gamma_T T}e^{+i(\omega_2-\omega_1)T}e^{-i\omega_1\tau}e^{+i\omega_2 t}\,\mathcal{F}\left\{e^{-\frac{\Delta\omega^2}{2\sigma^2}}\right\}\Big|_{t-\tau}$$

$$= \Theta(t)\Theta(T)\Theta(\tau)e^{-\gamma_1\tau}e^{-\gamma_2 t}e^{-\gamma_T T}e^{+i(\omega_2-\omega_1)T}e^{-i\omega_1\tau}e^{+i\omega_2 t}\left[e^{-\frac{\sigma^2}{2}t'^2}\right]_{t'=t-\tau}$$

$$= \Theta(t)\Theta(T)\Theta(\tau)e^{-\gamma_1\tau}e^{-\gamma_2 t}e^{-\gamma_T T}e^{+i(\omega_2-\omega_1)T}e^{-i\omega_1\tau}e^{+i\omega_2 t}e^{-\frac{\sigma^2}{2}(t-\tau)^2}$$

Shifting the frequency domain peak to the origin:

$$s_{origin}(t,T,\tau) = s(t,T,\tau)e^{-i(\omega_2-\omega_1)T}e^{-i\omega_2 t}$$

$$= \Theta(t)\Theta(T)\Theta(\tau)e^{-\gamma_1\tau}e^{-\gamma_2 t}e^{-\gamma_T T}e^{-i\omega_1\tau}e^{-\frac{\sigma^2}{2}(t-\tau)^2}$$

We project onto the *T* axis:

$$s_{proj}(T) = \int_{-\infty}^{\infty} s_{origin}(t,T,\tau)dt$$

$$= \Theta(t)\Theta(T)\Theta(\tau)e^{-\gamma_1\tau}e^{-\gamma_T T}e^{-i\omega_1\tau}\int_0^{\infty} e^{-\gamma_2 t}e^{-\frac{\sigma^2}{2}(t-\tau)^2}dt$$

$$= \Theta(t)\Theta(T)\Theta(\tau)e^{-(\gamma_1+\gamma_2)\tau}e^{-\gamma_T T}e^{-i\omega_1\tau}\int_{-\tau}^{\infty} e^{-\gamma_2 t'}e^{-\frac{\sigma^2}{2}t'^2}dt'$$

And taking the inhomogeneous limit:

$$s_{proj}(T) = \Theta(t)\Theta(T)\Theta(\tau)e^{-(\gamma_1+\gamma_2)\tau}e^{-\gamma_T T}e^{-i\omega_1\tau}$$

We obtain the frequency-domain lineshape:

$$S_{slice}(\omega_T) = \Theta(t)\Theta(\tau)e^{-(\gamma_1+\gamma_2)\tau}e^{-i\omega_1\tau}\mathcal{F}\{e^{-\gamma_T T}\Theta(T)\}$$
$$\propto \Theta(t)\Theta(\tau)e^{-(\gamma_1+\gamma_2)\tau}e^{-i\omega_1\tau}\frac{1}{\gamma_T - i\omega_T}$$

One-Quantum Lineshape Fits

The lineshapes observed in the obtained one-quantum spectra, especially on the $\Delta E < 0$ side of each spectra, exhibit lineshapes distorted by vibrational coupling that deviate from ideal summations of Lorentzians. We thus fit the co-linear and cross-linear lineshapes with symmetric complex Lorentzian peaks, but only on the $\Delta E \geq 0$ side.

Co-Linear Spectrum Fits

To investigate the dependence of parameters on nanocrystal size, we fit cross-diagonal slices centered at various slice positions $|\hbar\omega_\tau| = |\hbar\omega_t|$, shown in Fig. S4.

Cross-Linear Spectrum Fits

Just as with the co-linear spectrum, we fit cross-diagonal slices centered at various slice positions $|\hbar\omega_\tau| = |\hbar\omega_t|$, shown in Fig. S5.

Extracting the Optical Dephasing Rates

The slices are fitted in the range $0 \leq \Delta E \leq 2.5$ meV to five complex Lorentzians, where all four sidebands are shifted in phase by $\pi/2$ to achieve the correct lineshapes. To explore the possibility of a weak, third sideband at energy $\Delta E = \Omega_1 + \Omega_2$, corresponding to absorption and emission involving the states $|\psi_x\rangle$ and $|\psi_y\rangle$, we attempted to fit the above lineshapes with an additional two Lorentzian peaks. However, no reasonable fits were found possible.

From the fitted peak linewidths, we can extract the dephasing rates of the triplet state manifold γ_x, γ_y, and γ_z. To do so, we make the key assumption that the zero-phonon linewidth, which would be a weighted average of the three dephasing rates $\gamma_x, \gamma_y, \gamma_z$ for the case of equal strength dipole moments, is approximately equal to γ_y for the case of a stronger dipole moment d_y as discussed in the above section on peak strength calculations. This finally provides three equations and three variables. The dephasing rates are plotted in Fig. S6. While γ_x does not exhibit a clear monotonic increase or decrease with changing size, γ_y sharply increases at a slice position of around 1900 meV. This indicates that, within the size-distribution probed by our laser bandwidth, $|\psi_y\rangle$ becomes degenerate with $|\psi_d\rangle$ at an energy gap of around 1900 meV and becomes increasingly higher in energy at larger slice positions. A more statistically comprehensive study is needed to draw firm quantitative conclusions.

Co-Linear Zero-Quantum Spectra

Zero-quantum spectra were acquired with a co-linear (HHHH) excitation scheme, and shown in Fig. S7. No inter-triplet coherences were observed, which are expected to be symmetric in positive and negative mixing energy due to their electronic origin. However, multiple negative mixing energy sidebands appear with increasing delay τ, which we attribute to electronic-vibrational coupling and discuss in a separate paper.

Cross-Linear Zero-Quantum Spectra τ Dependence

Zero-quantum spectra were acquired with a cross-linear (HVHV) excitation scheme as a function of τ to confirm their electronic origin. Though the plot in Fig. 3B (in which each slice is normalized to its respective central peak) suggests a faster decay in sideband intensities relative to the central peak, this is not the case as shown by plots of the peak intensities in Fig. S8. The apparent faster decay of the sidebands is due to the overall decrease in signal to noise ratio of the measurements, and the increase in noise floor thus appears as an accelerated decrease in sideband intensity.

Correlation Between Inhomogeneously Broadened Transitions

We examine an alternative cause of line-broadening, namely partially-correlated inhomogeneous broadening between two optical transitions. To be more specific, we may define the two limiting cases of (1) perfectly correlated and (2) uncorrelated inhomogeneous broadening:

1. Perfectly correlated inhomogeneous broadening: all emitters that have a certain resonance energy for one optical transition will be degenerate with respect to the resonance energy of another optical transition. In other words, a change in resonance energy of an optical transition leads to a deterministic change in that of another.
2. Uncorrelated inhomogeneous broadening: emitters that have a certain resonance energy for one optical transition may assume a range of energies for a second optical transition with equal probability. The conditional probability of the second resonance energy (of an ensemble) is simply the inhomogeneous distribution of the respective optical transition.

In perovskite nanocrystals, partially-correlated inhomogeneous broadening may occur due to variations in anisotropy of the nanocrystal geometry. We thus examine the effect of such partial correlation on lineshapes in one-quantum spectra.

Model

To determine the effects of partially-correlated inhomogeneous broadening, we adopt a model introduced in (36). We begin with the rephasing signal resulting from excitation and emission frequencies ω_1 and ω_2 respectively of a single emitter:

$$R \propto e^{-i\omega_1\tau}e^{i\omega_2 t}e^{-\gamma_1\tau-\gamma_2 t}$$

We then define a generalized two-dimensional Gaussian function (ignoring normalization prefactors for clarity):

$$g(\omega_1,\omega_2) = e^{-\frac{4ln(2)}{(1-R^2)}\left[\frac{(\omega_1-\omega_1^c)^2}{\delta\omega_1^2}+\frac{(\omega_2-\omega_2^c)^2}{\delta\omega_2^2}-2R\frac{\omega_1-\omega_1^c}{\delta\omega_1}\frac{\omega_2-\omega_2^c}{\delta\omega_2}\right]}$$

where $\delta\omega_{1,2}$ are the FWHM of each inhomogeneous transition energy distribution, $\omega_{1,2}^c$ are the center energies of each distribution, and R is the correlation coefficient ranging from R = 0 (uncorrelated) to R = 1 (perfectly correlated).

To simplify the calculations, we follow (36) and define R and $\delta\omega_{1,2}$ in terms of the variables a_{11}, a_{22}, and a_{12}:

$$R = \frac{a_{12}}{\sqrt{a_{11}a_{22}}} \qquad \delta\omega_1 = \sqrt{\frac{4\ln(2)\,a_{11}}{a_{11}a_{22}-a_{12}^2}} \qquad \delta\omega_2 = \sqrt{\frac{4\ln(2)\,a_{22}}{a_{11}a_{22}-a_{12}^2}}$$

This recasts the distribution function as:

$$g(\omega_1,\omega_2) = e^{-a_{11}(\omega_1-\omega_1^c)^2}e^{-a_{22}(\omega_2-\omega_2^c)^2}e^{2a_{12}(\omega_2-\omega_2^c)(\omega_1-\omega_1^c)}$$

The rephasing signal generated from the inhomogeneous ensemble may then be calculated by:

$$\iint Rg(\omega_2,\omega_1)d\omega_2\, d\omega_1 = e^{i\omega_2^c t}e^{-i\omega_1^c \tau}e^{-\gamma_1\tau-\gamma_2 t}\iint e^{-iy\tau}e^{ixt}e^{-a_{11}x^2-a_{22}y^2+2a_{12}xy}$$

where we've defined x = ω_2-ω_2^c and y = ω_1-ω_1^c.

Since the following integral has the solution:

$$\iint e^{-\frac{1}{2}zAz+iJz}\,dz = \sqrt{\frac{(2\pi)^2}{\det|A|}}e^{-\frac{1}{2}JA^{-1}J}$$

We can define the following variables:

$$z = \begin{pmatrix} x \\ y \end{pmatrix} \qquad A = 2\begin{pmatrix} a_{11} & -a_{12} \\ -a_{12} & a_{22} \end{pmatrix} \qquad J = \begin{pmatrix} t \\ -\tau \end{pmatrix}$$

This recasts the above integral to provide the following solution:

$$\iint R(\omega_2,\omega_1,\tau,t)g(\omega_2,\omega_1)d\omega_2\, d\omega_1$$

$$\propto e^{i\omega_2^c t}e^{-i\omega_1^c \tau}e^{-\gamma_1\tau-\gamma_2 t}\iint e^{-\frac{1}{2}zAz+iJz}\,d\boldsymbol{z}$$

$$= \sqrt{\frac{(2\pi)^2}{4(a_{11}a_{22}-a_{12}^2)}}e^{i\omega_2^c t}e^{-i\omega_1^c \tau}e^{-\gamma_1\tau-\gamma_2 t}e^{-\frac{1}{4(a_{11}a_{22}-a_{12}^2)}[a_{22}t^2-2a_{12}\tau t+a_{11}\tau^2]}$$

and in terms of our original physical variables:

$$\iint R(\omega_2,\omega_1,\tau,t)g(\omega_2,\omega_1)d\omega_2\, d\omega_1$$

$$\propto e^{i\omega_2^c t}e^{-i\omega_1^c \tau}e^{-\gamma_1\tau-\gamma_2 t}e^{-\frac{\delta\omega_2^2}{16\ln(2)}[t^2-2R(\delta\omega_1/\delta\omega_2)t\tau+(\delta\omega_1/\delta\omega_2)^2\tau^2]}$$

Signatures in One-Quantum Spectra

To examine the signatures of partially-correlated inhomogeneous broadening in one-quantum spectra, we simulate sideband lineshapes according to the above model. To give a sense for parameters that would result in the broadening of sidebands 4 and 5 in Fig. 2D, we assume identical homogeneous dephasing rates between states $|\psi_y\rangle$ and $|\psi_z\rangle$ ($T_2^y = T_2^z$ = 5.32 ps). By fixing the inhomogeneous width ratio $\delta\omega_1/\delta\omega_2$ = 1 while varying the correlation parameter R, we obtain the following behavior for cross-diagonal slices of a single sideband located at ΔE = -Ω_1, plotted in Fig. S9.

We may quantify the changes by plotting the sideband intensity and effective dephasing rate with respect to correlation coefficient R, shown in Fig. S10. Just as uncorrelated inhomogeneous broadening suppresses quantum beats in integrated FWM measurements, the sideband intensity decreases sharply with decreasing correlation coefficient. This is due to incomplete rephasing of the photon echo signal without perfect correlation. The effective dephasing rate is calculated from the lineshape FWHM assuming the relationship for a normal Lorentzian lineshape. As expected, for R = 1 the effective dephasing time is simply the identical homogeneous dephasing rates used in the simulation ($T_2^y = T_2^z$ = 5.32 ps), and a correlation coefficient of approximately R = 0.98 is required to reach a broadening equivalent to the fitted experimental dephasing rate of $|\psi_z\rangle$ (T_2^z = 0.76 ps).

Supplementary Figures

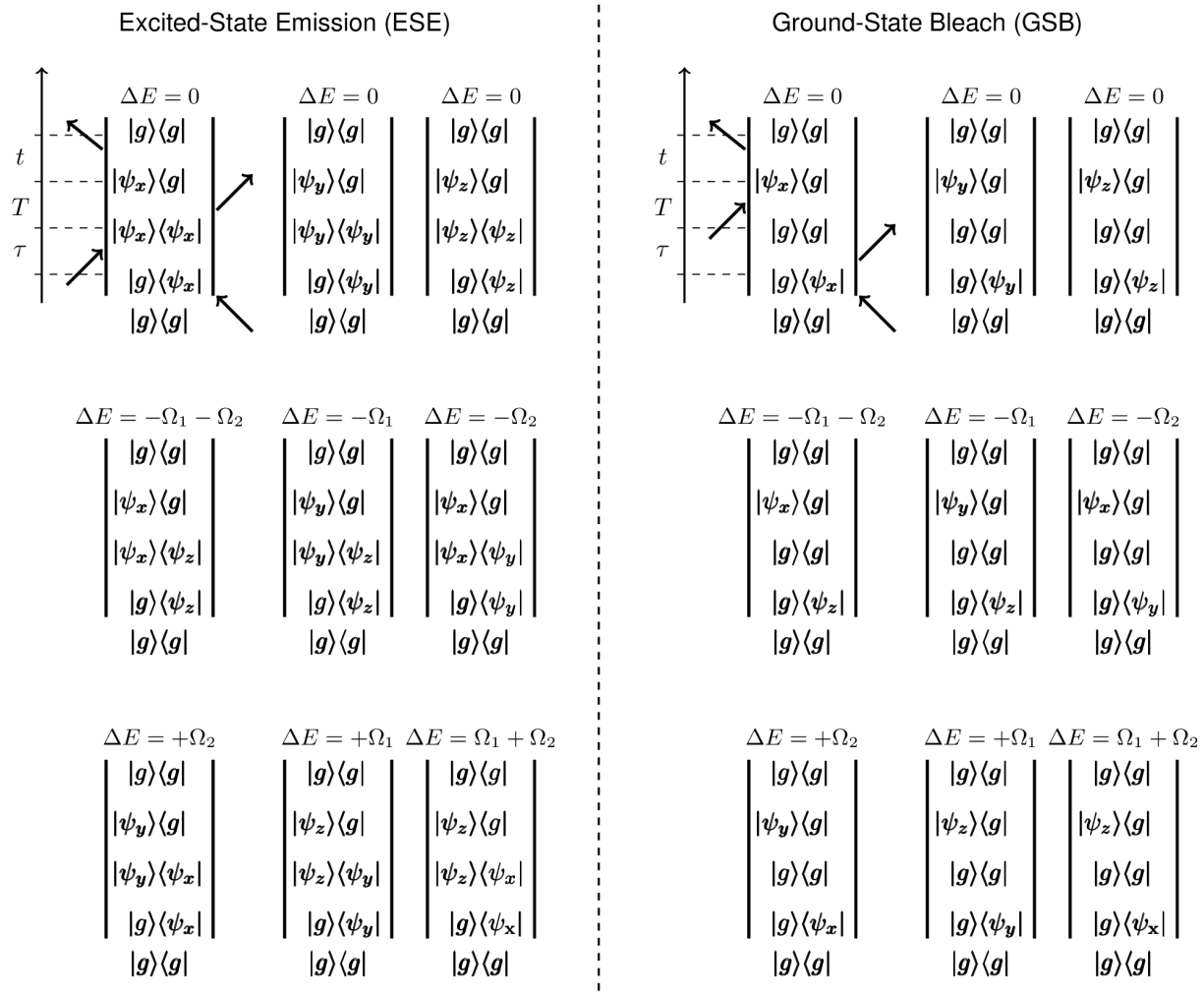

Fig. S1. Double-sided Feynman diagrams of quantum pathways. Double-sided Feynman diagrams representing accessible quantum pathways in perovskite nanocrystals. Nine ESE and GSB diagrams each are possible, which involve an intermediate excited-state population/coherence and ground-state population respectively. The peak position of each diagram in one-quantum spectra is labeled above. ESA diagrams are neglected as described in the text.

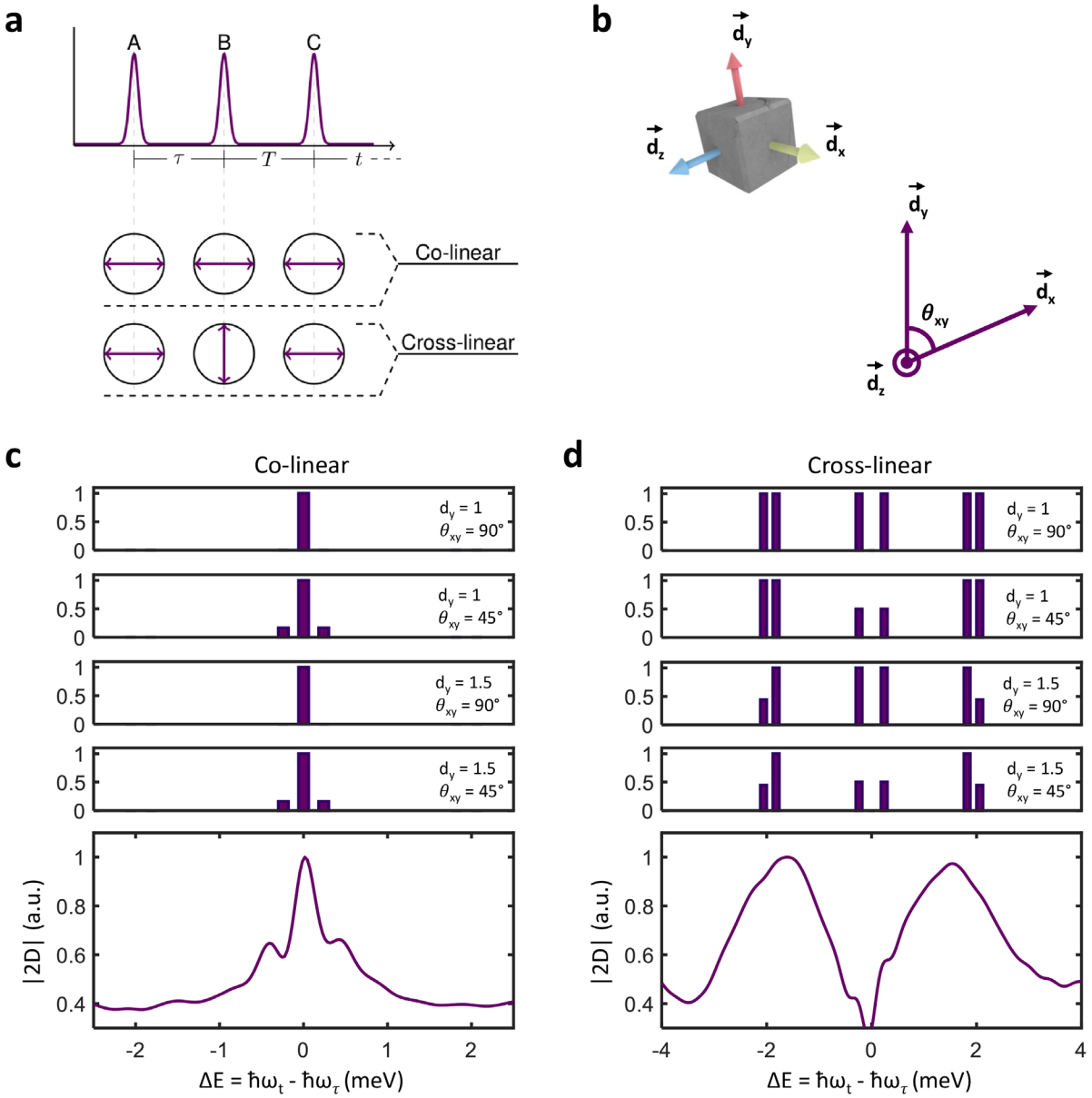

Fig. S2. Peak strength calculations. A, Excitation polarization sequences as described in Fig. 1D in the main text. **B**, Schematic of dipole moment vector orientations, in which $\vec{d}_z$ is mutually orthogonal to $\vec{d}_{x/y}$ while the angle θ_{xy} is allowed to vary. (**C, D)**, Calculated relative peak strengths for **C,** co-linear and **D,** cross-linear excitation for dipole matrix elements $\{d_x,d_y,d_z\} = \{1,d_y,1\}$ and angle θ_{xy} as indicated.

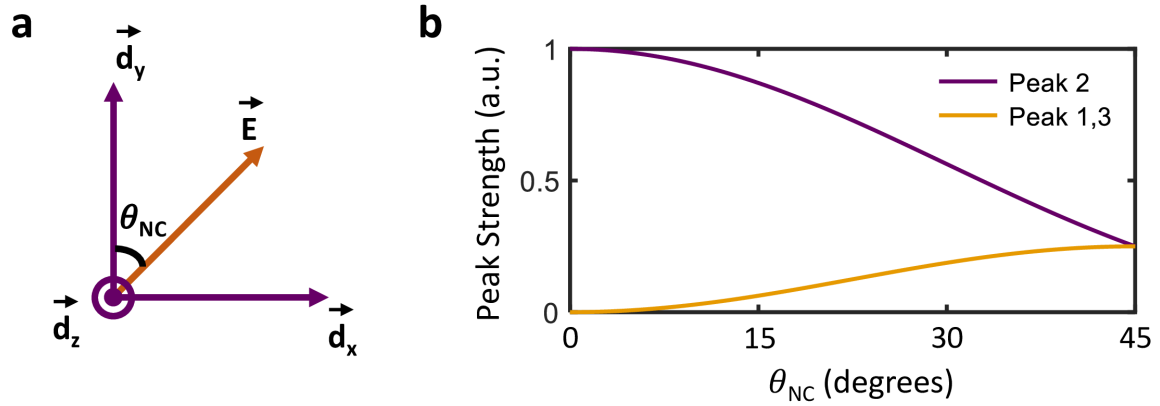

Fig. S3. Peak strength dependences on nanocrystal orientation. A, Nanocrystal orientation relative to the co-linear excitation pulse polarizations. **B**, Amplitudes of peaks 1-3 calculated for normalized dipole matrix elements $d_x = d_y = d_z = 1$ as a function of orientation angle θ_{NC}.

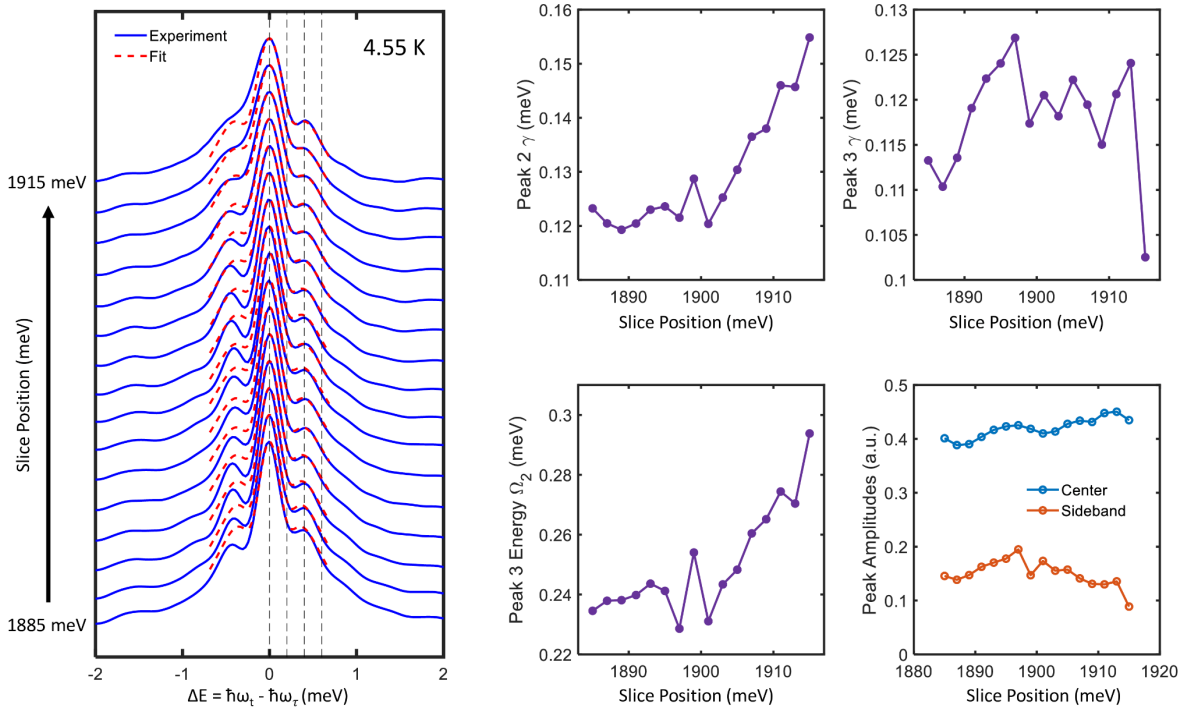

Fig. S4. Co-linear one-quantum lineshape fits. Left: The slices from a co-linear one-quantum spectrum at 4.6 K are plotted as blue curves, with their corresponding fitted lineshapes overlayed as dashed red lines. Right: Fitted parameters are plotted as a function of slice position.

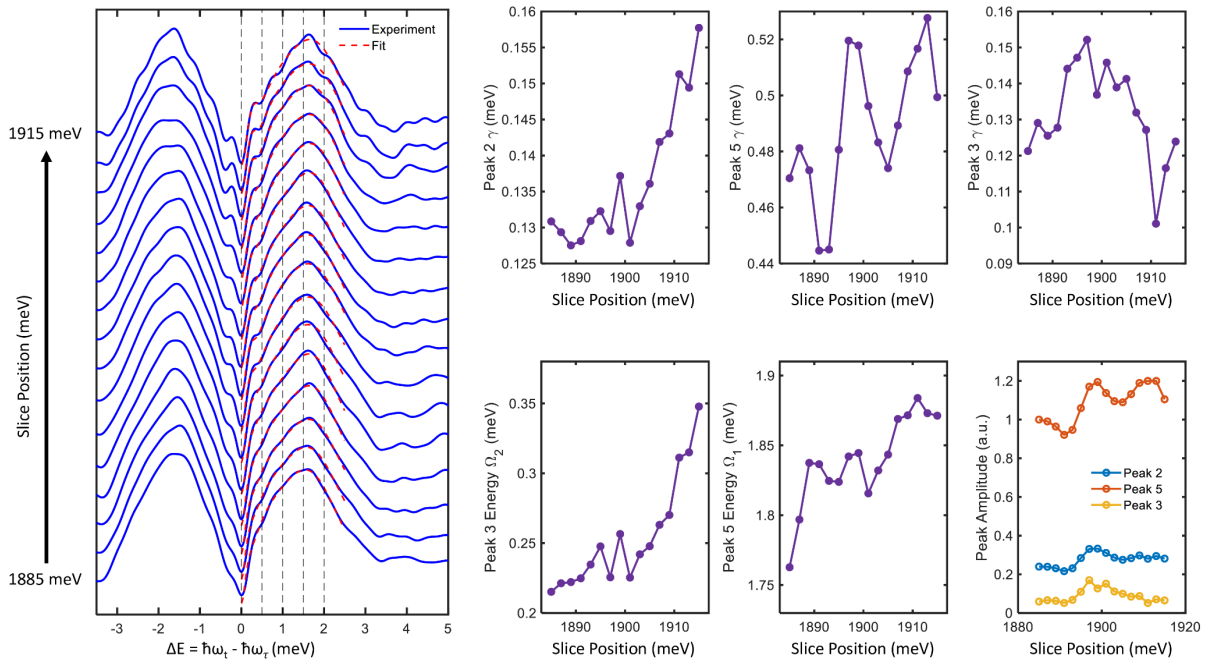

Fig. S5. Cross-linear one-quantum lineshape fits. Left: The slices from a cross-linear one-quantum spectrum at 4.6 K are plotted as blue curves, with their corresponding fitted lineshapes overlayed as dashed red lines. Right: Fitted parameters are plotted as a function of slice position.

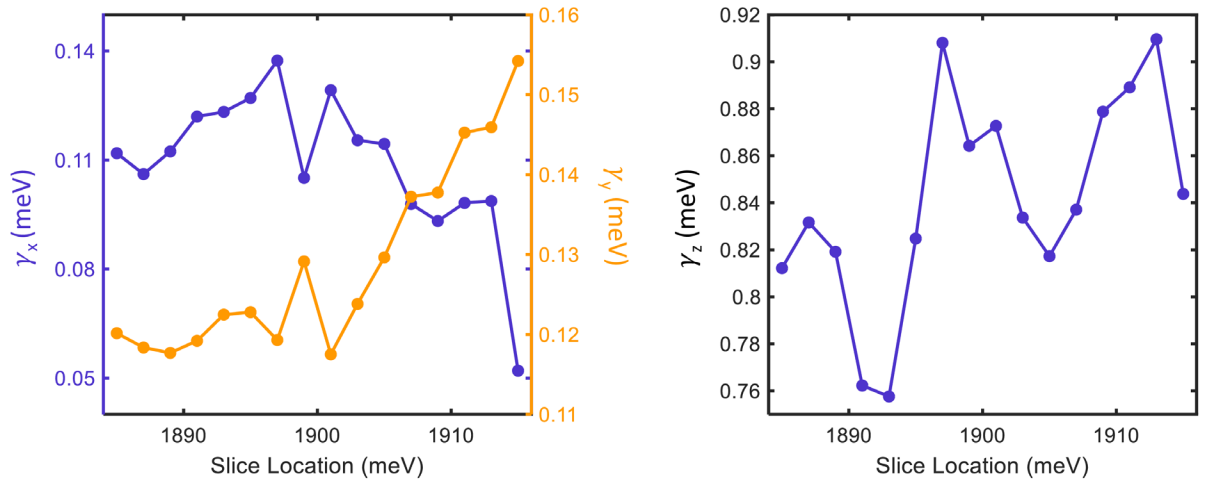

Fig. S6. Fitted optical dephasing rates. Individual dephasing rates of optical coherences extracted from fitted peak linewidths in co-linear and cross-linear one-quantum spectra.

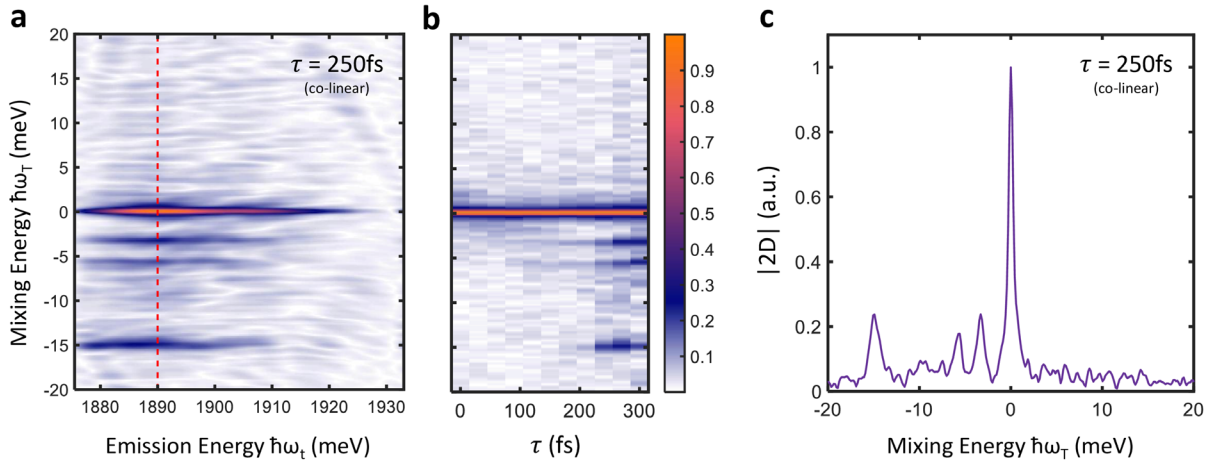

Fig. S7. Co-linear zero-quantum spectra. A, Zero-quantum spectra taken with co-linear excitation at $\tau = 250$ fs. **B**, Evolution of normalized slices taken at $\hbar\omega_t = 1890$ meV (indicated by the dashed red line in **A**). **C**, Normalized cross-slice taken at $\tau = 250$ fs and $\hbar\omega_t = 1890$ meV (indicated by the dashed red line in **A**).

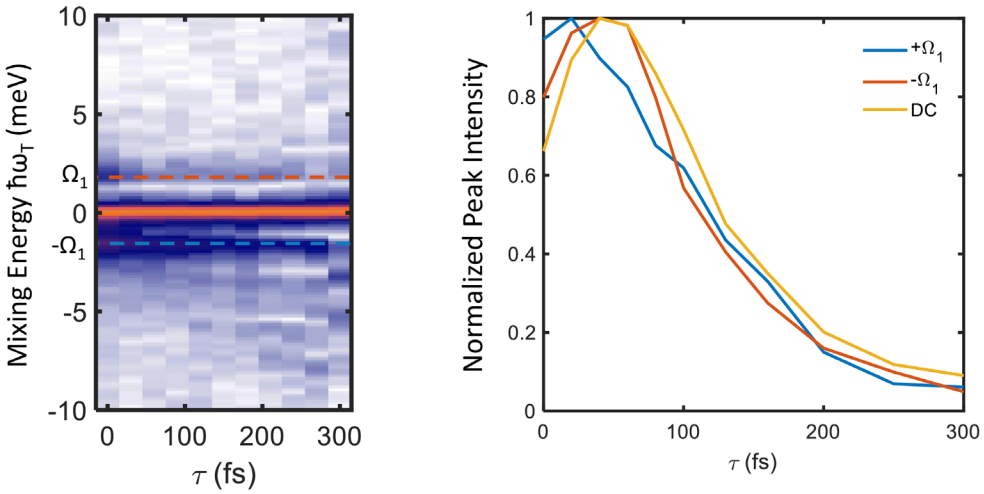

Fig. S8. Cross-linear zero-quantum spectra τ dependence. Peak intensities of the central (DC) peak and two sidebands as a function of τ, which decay at the same rate.

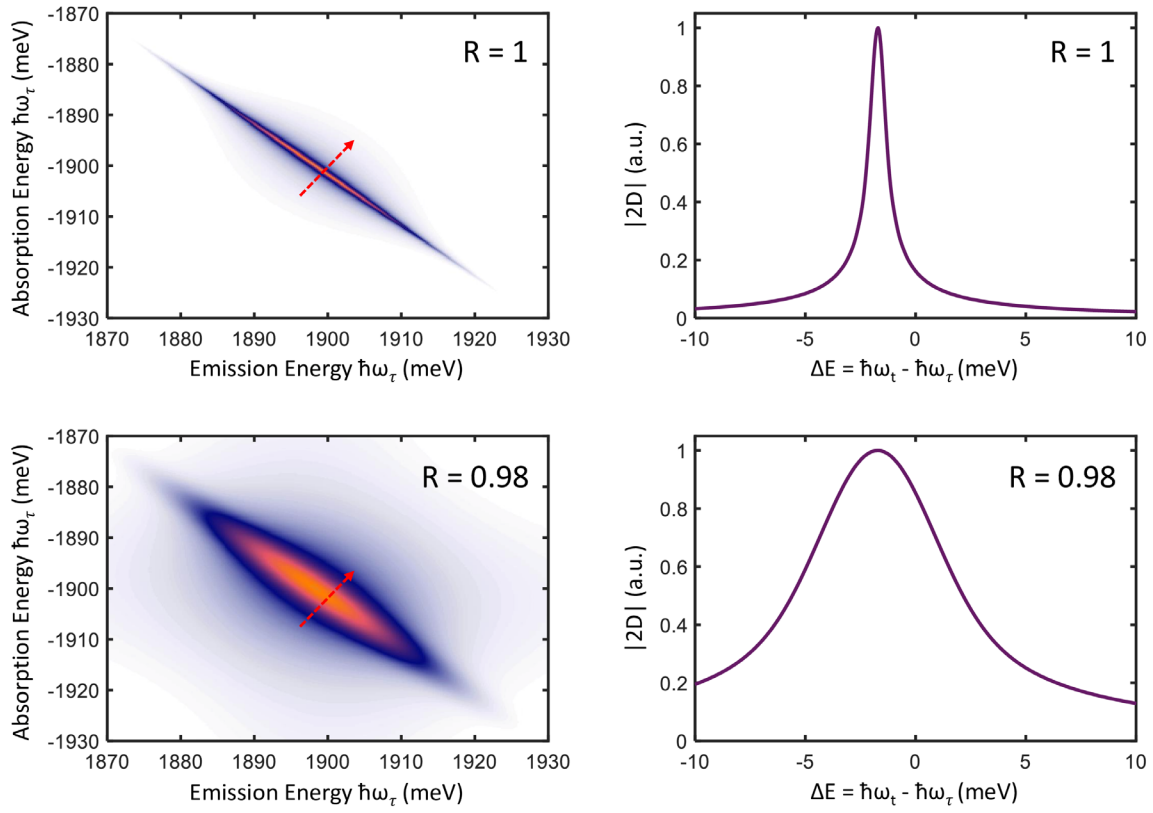

Fig. S9. One-quantum spectra with varying correlation coefficient. Left column: One-quantum spectra for a single sideband at $\Delta E = -\Omega_1$, simulated for correlation coefficients of R = 1 and R = 0.98 as indicated. Right column: Cross-diagonal slices of respective one-quantum spectra taken at $|\hbar\omega_\tau| = |\hbar\omega_t| = 1900$ meV as indicated by the red dashed arrows.

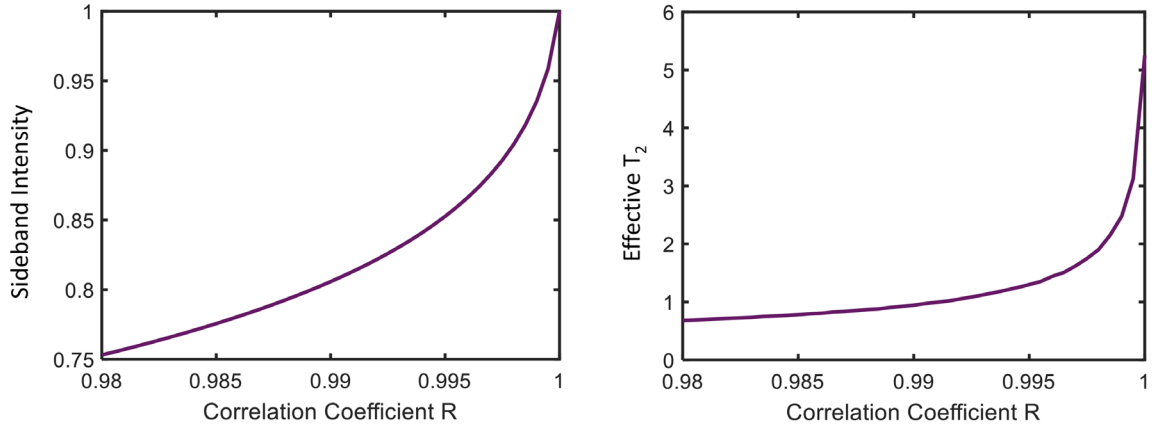

Fig. S10. Sideband intensity and linewidth with varying correlation coefficient. Integrated sideband intensity and effective dephasing time T_2 as a function of correlation coefficient R. Because the sideband lineshapes deviate from a Lorentzian lineshape with decreasing correlation coefficient, effective dephasing times are calculated from the Lorentzian FWHM relationship $\Delta E_{FWHM} = 4\gamma$.

REFERENCES AND NOTES

1. L. Protesescu, S. Yakunin, M. I. Bodnarchuk, F. Krieg, R. Caputo, C. H. Hendon, R. X. Yang, A. Walsh, M. V. Kovalenko, Nanocrystals of cesium lead halide perovskites ($CsPbX_3$, X = Cl, Br, and I): Novel optoelectronic materials showing bright emission with wide color gamut. *Nano Lett.* **15**, 3692–3696 (2015).

2. S.-T. Ha, R. Su, J. Xing, Q. Zhang, Q. Xiong, Metal halide perovskite nanomaterials: Synthesis and applications. *Chem. Sci.* **8**, 2522–2536 (2017).

3. F. Liu, Y. Zhang, C. Ding, S. Kobayashi, T. Izuishi, N. Nakazawa, T. Toyoda, T. Ohta, S. Hayase, T. Minemoto, K. Yoshino, S. Dai, Q. Shen, Highly luminescent phase-stable CsPbI3 perovskite quantum dots achieving near 100% absolute photoluminescence quantum yield. *ACS Nano*, **11**, 10373–10383 (2017).

4. J. Lim, B. G. Jeong, M. Park, J. K. Kim, J. M. Pietryga, Y.-S. Park, V. I. Klimov, C. Lee, D. C. Lee, W. K. Bae, Influence of shell thickness on the performance of light-emitting devices based on $CdSe/Zn_{1-X}Cd_XS$ core/shell heterostructured quantum dots. *Adv. Mater.* **26**, 8034–8040 (2014).

5. M. Nirmal, D. J. Norris, M. Kuno, M. G. Bawendi, A. L. Efros, M. Rosen, Observation of the “dark exciton” in CdSe quantum dots. *Phys. Rev. Lett.* **75**, 3728–3731 (1995).

6. M. A. Becker, R. Vaxenburg, G. Nedelcu, P. C. Sercel, A. Shabaev, M. J. Mehl, J. G. Michopoulos, S. G. Lambrakos, N. Bernstein, J. L. Lyons, T. Stöferle, R. F. Mahrt, M. V. Kovalenko, D. J. Norris, G. Rainò, A. L. Efros, Bright triplet excitons in caesium lead halide perovskites. *Nature* **553**, 189–193 (2018).

7. P. Tamarat, M. I. Bodnarchuk, J.-B. Trebbia, R. Erni, M. V. Kovalenko, J. Even, B. Lounis, The ground exciton state of formamidinium lead bromide perovskite nanocrystals is a singlet dark state. *Nat. Mater.* **18**, 717–724 (2019).

8. G. Rainò, M. A. Becker, M. I. Bodnarchuk, R. F. Mahrt, M. V. Kovalenko, T. Stöferle, Superfluorescence from lead halide perovskite quantum dot superlattices. *Nature* **563**, 671–675 (2018).

9. H. Utzat, W. Sun, A. E. K. Kaplan, F. Krieg, M. Ginterseder, B. Spokoyny, N. D. Klein, K. E. Shulenberger, C. F. Perkinson, M. V. Kovalenko, M. G. Bawendi, Coherent single-photon emission from colloidal lead halide perovskite quantum dots. *Science* **363**, 1068–1072 (2019).

10. C. Yin, L. Chen, N. Song, Y. Lv, F. Hu, C. Sun, W. W. Yu, C. Zhang, X. Wang, Y. Zhang, M. Xiao, Bright-exciton fine-structure splittings in single perovskite nanocrystals. *Phys. Rev. Lett.* **119**, 026401 (2017).

11. L. Chen, B. Li, C. Zhang, X. Huang, X. Wang, M. Xiao, Composition-dependent energy splitting between bright and dark excitons in lead halide perovskite nanocrystals. *Nano Lett.* **18**, 2074–2080 (2018).

12. N. S. Makarov, S. Guo, O. Isaienko, W. Liu, I. Robel, V. I. Klimov, Spectral and dynamical properties of single excitons, biexcitons, and trions in cesium-lead-halide perovskite quantum dots. *Nano Lett.* **16**, 2349–2362 (2016).

13. J. A. Castañeda, G. Nagamine, E. Yassitepe, L. G. Bonato, O. Voznyy, S. Hoogland, A. F. Nogueira, E. H. Sargent, C. H. Brito Cruz, L. A. Padilha, Efficient biexciton interaction in perovskite quantum dots under weak and strong confinement. *ACS Nano* **10**, 8603–8609 (2016).

14. G. Moody, C. K. Dass, K. Hao, C.-H. Chen, L.-J. Li, A. Singh, K. Tran, G. Clark, X. Xu, G. Berghäuser, E. Malic, A. Knorr, X. Li, Intrinsic homogeneous linewidth and broadening mechanisms of excitons in monolayer transition metal dichalcogenides. *Nat. Commun.* **6**, 8315 (2015).

15. K. Hao, G. Moody, F. Wu, C. K. Dass, L. Xu, C.-H. Chen, L. Sun, M.-Y. Li, L.-J. Li, A. H. Mac Donald, X. Li, Direct measurement of exciton valley coherence in monolayer WSe_2. *Nat. Phys.* **12**, 677–682 (2016).

16. A. Liu, D. B. Almeida, W. K. Bae, L. A. Padilha, S. T. Cundiff, Non-markovian exciton-phonon interactions in core-shell colloidal quantum dots at femtosecond timescales. *Phys. Rev. Lett.* **123**, 057403 (2019).

17. A. Liu, D. B. Almeida, W.-K. Bae, L. A. Padilha, S. T. Cundiff, Simultaneous existence of confined and delocalized vibrational modes in colloidal quantum dots. *J. Phys. Chem. Lett.* **10**, 6144–6150 (2019).

18. S. T. Cundiff, S. Mukamel, Optical multidimensional coherent spectroscopy. *Phys. Today* **66**, 44–49 (2013).

19. J. R. Schaibley, H. Yu, G. Clark, P. Rivera, J. S. Ross, K. L. Seyler, W. Yao, X. Xu, Valleytronics in 2D materials. *Nat. Rev. Mater.* **1**, 16055 (2016).

20. A. D. Bristow, D. Karaiskaj, X. Dai, T. Zhang, C. Carlsson, K. R. Hagen, R. Jimenez, S. T. Cundiff, A versatile ultrastable platform for optical multidimensional Fourier-transform spectroscopy. *Rev. Sci. Instrum.* **80**, 073108 (2009).

21. S. Mukamel, *Principles of Nonlinear Optical Spectroscopy* (Oxford Univ. Press, ed. 1, 1999).

22. H. Seiler, S. Palato, C. Sonnichsen, H. Baker, E. Socie, D. P. Strandell, P. Kambhampati, Two-dimensional electronic spectroscopy reveals liquid-like lineshape dynamics in $CsPbI_3$ perovskite nanocrystals. *Nat. Commun.* **10**, 4962 (2019).

23. W. Zhao, Z. Qin, C. Zhang, G. Wang, X. Huang, B. Li, X. Dai, M. Xiao, Optical gain from biexcitons in $CsPbBr_3$ nanocrystals revealed by two-dimensional electronic spectroscopy. *J. Phys. Chem. Lett.* **10**, 1251–1258 (2019).

24. F. V. A. Camargo, T. Nagahara, S. Feldmann, J. M. Richter, R. H. Friend, G. Cerullo, F. Deschler, Dark subgap states in metal-halide perovskites revealed by coherent multidimensional spectroscopy. *J. Am. Chem. Soc.* **142**, 777–782 (2020).

25. L. Yang, T. Zhang, A. D. Bristow, S. T. Cundiff, S. Mukamel, Isolating excitonic Raman coherence in semiconductors using two-dimensional correlation spectroscopy. *J. Chem. Phys.* **129**, 234711 (2008).

26. M. E. Siemens, G. Moody, H. Li, A. D. Bristow, S. T. Cundiff, Resonance lineshapes in two-dimensional Fourier transform spectroscopy. *Opt. Express*, **18**, 17699–17708 (2010).

27. A. Liu, S. T. Cundiff, Spectroscopic signatures of electron-phonon coupling in silicon-vacancy centers in diamond. *Phys. Rev. Mater.* **4**, 055202 (2020).

28. K. Hao, J. F. Specht, P. Nagler, L. Xu, K. Tran, A. Singh, C. K. Dass, C. Schüller, T. Korn, M. Richter, A. Knorr, X. Li, G. Moody, Neutral and charged inter-valley biexcitons in monolayer $MoSe_2$. *Nat. Commun.* **8**, 15552 (2017).

29. M. A. Becker, L. Scarpelli, G. Nedelcu, G. Rainò, F. Masia, P. Borri, T. Stöferle, M. V. Kovalenko, W. Langbein, R. F. Mahrt, Long exciton dephasing time and coherent phonon coupling in $CsPbBr_2Cl$ perovskite nanocrystals. *Nano Lett.* **18**, 7546–7551 (2018).

30. K. B. Ferrio, D. G. Steel, Raman quantum beats of interacting excitons. *Phys. Rev. Lett.* **80**, 786–789 (1998).

31. S. Haessler, J. Caillat, W. Boutu, C. Giovanetti-Teixeira, T. Ruchon, T. Auguste, Z. Diveki, P. Breger, A. Maquet, B. Carré, R. Taïeb, P. Salières, Attosecond imaging of molecular electronic wavepackets. *Nat. Phys.* **6**, 200–206 (2010).

32. P. C. Sercel, J. L. Lyons, D. Wickramaratne, R. Vaxenburg, N. Bernstein, A. L. Efros, Exciton fine structure in perovskite nanocrystals. *Nano Lett.* **19**, 4068–4077 (2019).

33. F. Langer, C. P. Schmid, S. Schlauderer, M. Gmitra, J. Fabian, P. Nagler, C. Schüller, T. Korn, P. G. Hawkins, J. T. Steiner, U. Huttner, S. W. Koch, M. Kira, R. Huber, Lightwave valleytronics in a monolayer of tungsten diselenide. *Nature* **557**, 76–80 (2018).

34. A. Liu, L. G. Bonato, F. Sessa, D. B. Almeida, E. Isele, G. Nagamine, L. F. Zagonel, A. F. Nogueira, L. A. Padilha, S. T. Cundiff, Effect of dimensionality on the optical absorption properties of $CsPbI_3$ perovskite nanocrystals. *J. Chem. Phys.* **151**, 191103 (2019).

35. G. Scholes, Selection rules for probing biexcitons and electron spin transitions in isotropic quantum dot ensembles. *J. Chem. Phys.* **121**, 10104–10110 (2004).

36. S. T. Cundiff, Effects of correlation between inhomogeneously broadened transitions on quantum beats in transient four-wave mixing. *Phys. Rev. A* **49**, 3114–3118 (1994).